Title

Elastic thickness and heat flux estimates for the uranian satellite Ariel

Journal

Icarus, 250

ISSN

00191035

Authors

Peterson, G.
Nimmo, F.
Schenk, P.

Publication Date

2015-04-01

DOI

10.1016/j.icarus.2014.11.007

Peer reviewed

Elastic thickness and heat flux estimates for the Uranian satellite Ariel

G. Peterson, gpeterso@ucsc.edu
F. Nimmo,Department of Earth and Planetary Sciences University of California Santa Cruz, 95064,fnimmo@es.ucsc.edu ,
P. Schenk, Lunar and Planetary Institute, 3600 Bay Area Blvd., Houston, Texas 77058
schenk@lpi.usra.edu

Abstract

The surface of Ariel, an icy satellite orbiting Uranus, shows extensional tectonic features suggesting an episode of endogenic heating in the satellite's past. Using topography derived from stereo-photoclinometry, we identified flexural uplift at a rift zone suggesting elastic thickness values in the range 3.8-4.4 km. We estimate the temperature at the base of the lithosphere to be in the range **99 to 146** K, depending on the strain rate assumed, with corresponding heat fluxes of **28-92** mW/m^2. Neither tidal heating, assuming Ariel's current eccentricity, nor radiogenic heat production from the silicate core are enough to cause the inferred heat fluxes. None of three proposed ancient mean-motion resonances produce equilibrium tidal heating values in excess of 4.3 mW/m^2. Thus, the origin of the inferred high heat fluxes is currently mysterious.

Keywords: Uranus, Ariel, Satellites, Thermal history, Planetary Science

Highlights:

- Flexural rift flank uplift is identified on Ariel
- The inferred elastic thickness is used to estimate heat fluxes
- The heat fluxes are larger than can be produced by **equilibrium** tidal heating

1. Introduction

There are five classical satellites in the Uranian system: Miranda, Ariel, Umbriel, Titania, and Oberon. Like those of the Saturnian system, their bulk densities vary irregularly with distance from the planet. Ariel is the 4th largest with a radius of 579 km and a fairly high bulk density of 1660 kg/m^3 (Peale, 1999), implying a mixed composition of silicate rock and ice. The internal structure of Ariel is uncertain, but it is plausible that heat fluxes were once high enough to allow differentiation after accretion, based on the observed icy surface and deformation present (**Hussmann et al., 2006**). Its internal structure may therefore consist of a rocky core surrounded by a layer of ice. Assuming a core density of 3500 kg/m^3 and an ice density of 930 kg/m^3, Ariel's core would be 380 km in radius.

Voyager 2 was the first spacecraft to image Ariel's surface, providing observational evidence of resurfacing. Most of the images taken are of the southern hemisphere and of the side facing Uranus in its synchronous orbit; only 35% percent of Ariel was viewed in total (Plescia and Boyce, 1987). Ariel has been divided into three terrains (cratered, ridges and plains), all of which can be seen in Figure 1a. Cratered terrain makes up the largest portion; it is found between the younger cross-cutting grabens and is associated with albedo variations, possibly from ejecta debris (Plescia and Boyce, 1987). Unlike Oberon and Umbriel, Ariel has few very large craters **in the visible region**. One of the larger complex craters, Yangoor, is about 80 km in diameter *D* with part of the crater covered by younger terrain (Miller, 1998). Crater density studies suggest that none of the observed surfaces are as old as Umbriel or Oberon, whose surfaces date back to the heavy bombardment. Crater densities on these two satellites are about 1800 per 10^6 km^2($D \geq 30$km) (Plescia and Boyce, 1987). However, crater frequencies found on Ariel are significantly lower, about 32 per 10^6 km^2 ($D \geq 30$km) (Plescia and Boyce, 1987), strongly suggesting that Ariel has undergone significant resurfacing. Schenk and McKinnon (1988) identified several craters that are anomalously shallow, about 50-70% of the depth of more recent craters. These characteristics are indicative of viscous relaxation of the icy crust and suggest high heat fluxes, which is consistent with the observed resurfacing.

The smooth areas with few craters are termed plains and are associated with apparently extruded material found on the floor of grabens. The flooded valley floors are convex, suggesting they formed from material with high viscosity (Schenk, 1989). It is thought that vertical mobilization of warmer solid-state material may have resulted in the inferred extrusion and

would require high heat fluxes (Schenk, 1989). **However, we note that early interpretations of cryovolcanism on Jovian and Saturnian satellites based on low-resolution images have generally not been supported by later, higher-resolution images (Johnson, 2005). Some caution is therefore required in interpreting terrains on Ariel as cryovolcanic.**

The grabens form extensive networks of parallel faulting, suggesting an episode of extensional tectonics (Plescia and Boyce, 1987).**Whether or not the surface viewed by *Voyager* represents global or regional deformation is unknown. Nonetheless, the existence of the largest canyon, Kachina Chasmata, which extends for 500 km, suggests that extension was not simply a local phenomenon. Based on the regional deformation observed,** Nyffenegger et al. (1997) argued that the faulting seen on Ariel is not consistent with a global volume change from refreezing of an ocean, as the orientation of faults shifts slightly clockwise across the surface of Ariel, suggestive of tidal flexing. Significant tidal stresses could have been generated during episodes of high orbital eccentricity, consistent with the many possible resonances that Ariel may have encountered (Tittemore and Wisdom 1989; Tittemore, 1990).

Observed ridges on Ariel are generally oriented east or north-east. The similarity of their height, width and orientation **to the grabens** suggest that these ridges formed via similar geological processes (Plescia and Boyce, 1987). **Ariel's ridged topography is comparable to the parallel-ridged terrain seen on Ganymede. The morphology of Ganymede's parallel ridge units is suggestive of an extensional environment, where horst-and-graben style normal faulting has been suggested as the principal process shaping these ridges (Pappalardo et al., 1998).** As on Ganymede, Ariel's ridge terrain and grabens both crosscut the cratered terrain indicating that they are geologically younger. Additionally, cratering densities at graben and ridged terrain are similar, suggesting both formed during the same episode of tectonic activity (Plescia and Boyce, 1987). Overall, Ariel's geology suggests a period of global resurfacing after accretion, deforming the original crust. The cratered terrain formed first, followed by graben formation triggered by an endogenic heat source, which additionally caused viscous relaxation of remaining craters and possibly warm ice to extrude from graben floors (Schenk, 1991).

In this paper, we investigate the thermal history of Ariel by analyzing surface features. Topography places loads on an ice shell which can be supported either by the strength of the

elastic plate or the buoyancy force due to displaced low-density material. Estimates of the elastic thickness allow calculations of local thermal gradients and, thus, heat fluxes, at the time the terrain formed (e.g. Nimmo et al., 2002), although these estimates may be affected by long-term relaxation (Damptz and Dombard 2011). Modeling observed topographic profiles as flexural (elastically-supported) features has been applied to several other icy satellites as well. These include Europa, Tethys, Ganymede, Enceladus and Dione (Hurford et al. 2005, Billings and Kattenhorn 2005, Giese et al. 2007, Nimmo and Pappalardo 2004, Giese et al. 2008, Hammond et. al 2013).

Currently, the Uranian satellites remain largely unexplored. So far, there have been no attempts to use topographic data on Ariel to estimate heat fluxes, although a study of Miranda rift flank topography from limb profiles yielded an effective elastic thickness of about 2 km (Pappalardo et al. 1997). The present-day Uranian system differs from the Galilean and Saturnian systems in that none of its satellites are currently in stable orbital resonances. Past papers on Ariel have investigated potential mean motion resonance configurations with the other satellites to isolate a heat source that could explain the inferred resurfacing (Dermott et. al 1988, Tittemore and Wisdom 1989, Tittemore 1990). However, below we conclude that neither Ariel's present eccentricity, nor radioactive heating, nor any of the previously calculated ancient resonances (2:1 with Umbriel, 5:3 with Miranda, or 4:1 with Titania) are sufficient to explain the inferred heat fluxes.

The approach that we employ below to estimate heat fluxes based on elastic thickness estimates is highly simplified compared to more sophisticated, finite-element techniques (e.g. Dombard and McKinnon 2006). Our rationale for adopting this approach is twofold. First, fitting a simple elastic profile allows comparison with the large body of pre-existing literature on icy satellite flexure. Even though all such studies neglect the potential role of long-term relaxation of topography (Damptz and Dombard 2011), relaxation is unlikely to change the *relative* amplitudes of heat flux inferred for different bodies. Second, the surface of Ariel is sufficiently poorly characterized, and the uncertainties (e.g. in the duration of rifting) sufficiently large, that employing a more sophisticated model is hard to justify.

2. Data

Figure 1a is an image mosaic of Ariel's icy surface between 270-360° E longitude and 0-60° S latitude. It shows the wide flat grabens and lack of craters, consistent with relatively recent extensional tectonics. Figure 1b shows topography derived from stereo-photoclinometry for the same area, using the same method as described in Schenk (1989). **The topographic data are derived using a combination of stereo and photoclinometry (shape-from-shading) techniques (e.g., Schenk and Pappalardo, 2004; Schenk, 2009). We use *Voyager* images 2684338 as the left-hand and 2684535 and 2684537 as the right-hand images. The stereo digital elevation model (DEM) is produced using an ISIS-based stereo scene-matching algorithm used successfully on other icy satellites, and for this stereo geometry gives a nominal stereo vertical precision of ~150m. Because a scene-recognition method is used and because of smear in one of the images, each measurement has a horizontal spot size or resolution of 5 pixels, or 5 km on Ariel.**

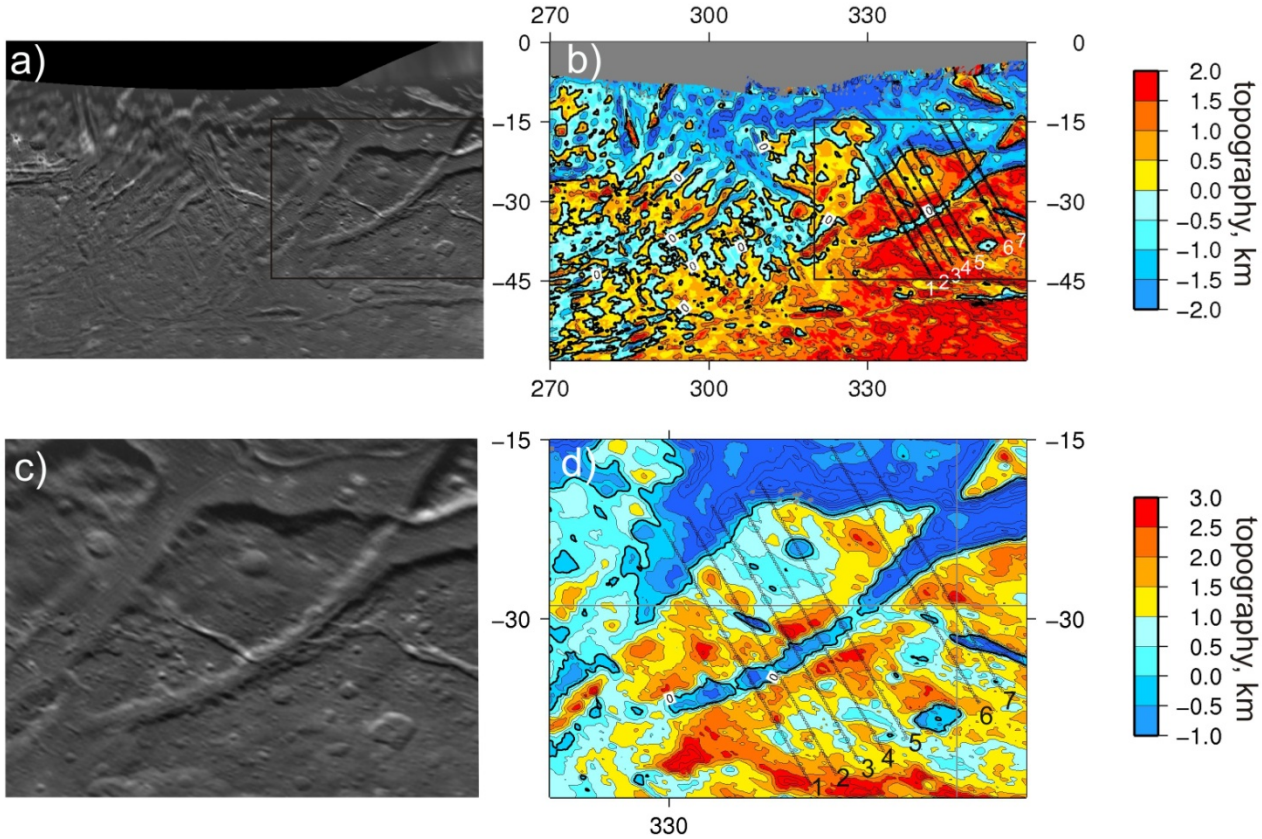

Figure 1.a) Image mosaic taken by *Voyager 2* of a portion of Ariel's surface illustrating the deformation of its icy exterior and young surface age. Simple cylindrical projection; 1° of latitude equals 10.1 km. The image is between 270-360° E longitude and 0 to 60°S latitude. Box outline denotes the zoomed-in portion shown in c) and d). b) Simple cylindrical projection of stereo-photoclinometry-derived topography from the image shown in a) with a contour

interval of 1km. Lines 1-7 indicate the location of the profiles extracted (see Fig 2). c) Zoomed-in portion of a). d) Zoomed-in portion of b). Contour internal 0.5 km; note the different colour scale.

The 2-dimensional photoclinometry DEM component calculates slopes at every pixel in the map, with a horizontal resolution of 1 km. *Voyager* images 2684535, 2684537, 2684539, 2684541 were used. Heights are integrated along horizontal profiles to produce a surface map of elevation (e.g., Schenk, 2009). The PC-DEM improves the vertical resolution of the final product by adding high-frequency information. While the uncertainties in each photoclinometry-derived slope value are quite small (<5%), they are unique to each pixel, and any uncertainties in absolute heights and slopes for each pixel are propagated along each line such that errors accumulate in a complex manner (e.g. Jankowski and Squyres 1991). In any case, the stereo component (which covers identical terrain) is used to divide out the long-wavelength component of the photoclinometry DEM, while preserving the high-frequency information within it. The final merged DEM has a horizontal resolution of 1 km and a vertical resolution of 150 meters or better.

To test the dependency of our result on the photoclinimetric component, and to get an indication of the likely uncertainties, we directly compare profiles from the stereo-DEM and the stereo-PC-DEM . This comparison is shown in Fig 2 below. Regardless of the inherent quality of the PC-DEM, our comparison shows that the long-wavelength components are very well preserved within the DEM and more than sufficient to characterize the grabens on Ariel.

3. Method

The larger graben we study here are much wider than the intrinsic stereo resolution (5 km) and show consistent structure along strike in Fig 1b, indicating that they are adequately resolved. We focused on the graben flanks, which often show uplift due to unloading of the lithosphere during crustal extension (e.g. Weissel et al., 1989, Pappalardo et al., 1997). In particular we analyzed a large graben, as highlighted by Figure 1b and d, located around 350˚ longitude and 30˚S latitude. **Fig 1d shows consistent-along strike topography indicative of rift-flank uplift on both sides of the rift.**

Figure 2 shows seven successive topographic profiles taken approximately perpendicular to the strike using both the stereo-PC-DEM (Fig 2a) and the stereo-DEM (Fig 2b) . In many cases rift flank uplift with curvature suggesting a flexural response is observed; particularly clear examples are highlighted with arrows. In some cases there is also a long-wavelength trend. Whether these trends are real remains uncertain due to the fact that we do not have an adequate global shape model. These profiles were then summed together to find an average profile for the graben. The width of the uplifted region for the averaged profile is then an indication of the flexural parameter, α, at the time of formation (e.g. Hammond et al., 2013). **The long linear extent of the graben-bounding faults (Fig 1c) suggest that they have penetrated the entire elastic layer.**

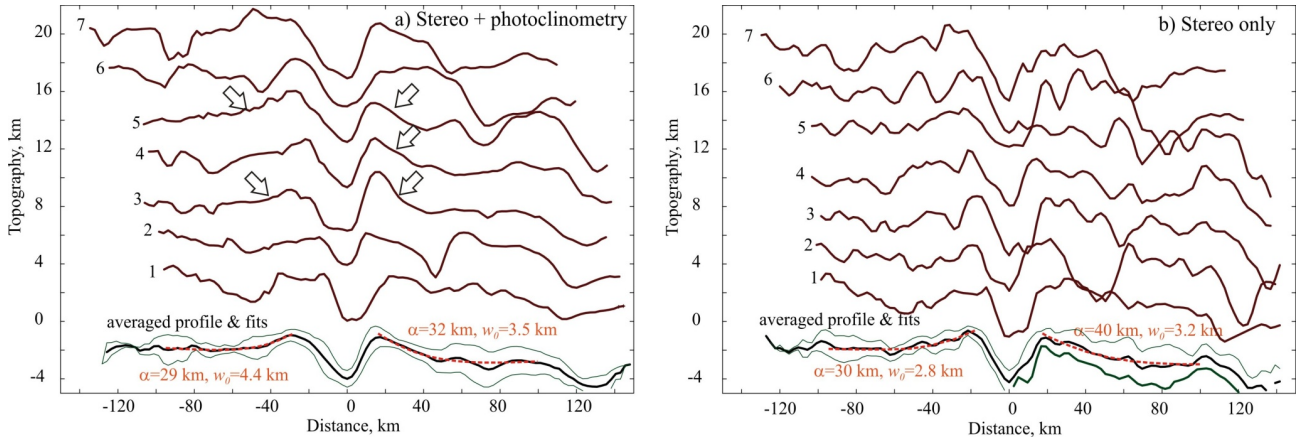

Figure 2. a) and b) each show the 7 successive topographic profiles extracted from the locations plotted in Figure 1b, except that a) was derived from a stereo-PC-DEM and b) was derived from a stereo-only DEM (see text). Arrows in a) highlight profiles showing apparent flexural curvature. The bottom-most profile in each graph is derived by averaging profiles 1-7. Green lines are +/- one standard deviation. Red dashed lines are theoretical fits (equation 1) to the averaged profile obtained by varying α and w_0 to find the minimum misfit. Note that the inferred flexural parameters α are almost identical for the two DEMs employed.

For a broken elastic plate, the deformation w in response to a line load is given by (e.g. Turcotte and Schubert 2002):

$$w = w_0 \exp\left(-\frac{x}{\alpha}\right)\cos\left(\frac{x}{\alpha}\right) \quad (1)$$

where w_0 is the deflection at x=0. **Assuming a broken plate results in higher elastic thicknesses and thus lower heat fluxes than an intact plate, and therefore represents a conservative choice.**

Equation (1) was applied separately to the two halves of the averaged profiles in Figure 2 to derive the minimum-misfit value for α and w_0 (see Figure 2). Fitting individual profiles (e.g. profile 3) would yield somewhat smaller values of α, and thus imply higher heat fluxes; to provide a conservative (lower bound) estimate of the heat fluxes, we therefore use α derived from the averaged profile. **We also note that the value of α derived is almost the same for the stereo-only and PC-stereo DEM's, indicating that our approach is robust.**

The quantity α is related to the local elastic thickness t_e by (Turcotte and Schubert 2002):

$$\alpha = \left(\frac{E t_e^3}{3(1-\nu^2)\Delta\rho g} \right)^{\frac{1}{4}} \quad (2)$$

where E is the Young's modulus, ν is the poisson's ratio, g is the gravitational acceleration on Ariel, and $\Delta\rho$ is the density difference between the shell and the overlying material (which in this case is vacuum). The Young's modulus and the Poisson's ratio of intact ice are 9 GPa and 0.33, respectively (Gammon et al. 1983). The values used are summarized in Table 1.

4. Results

For the rest of this paper, we will adopt the flexural parameter derived from the stereo-PC-DEM , which ranges from 29 and 32 km, implying elastic thicknesses between 3.8-4.4 km (equation 2). To find the resulting heat fluxes when the rift formed requires determining the thermal gradient. To do so, we estimate the temperature at the base of the elastic layer, T_b with the following equation (Nimmo et al. 2002):

$$T_b = \frac{Q_a}{nR} \left[\ln \left(\frac{3De\mu A^{\frac{1}{n}}}{\dot{\varepsilon}^{\frac{1}{n}} d^{\frac{p}{n}}} \right) \right]^{-1} \quad (3)$$

The elastic layer temperature, T_b, is dependent on the rheological behavior of ice, Q_a being the activation energy for ice creep, A the material parameter, and n and p the stress and grain size exponents. These dynamical properties are determined by creep experiments. Using a wide range of stress, strain rate, and temperature values, Goldsby and Kohlstedt (2001) identified three different deformation mechanisms, dislocation creep, grain boundary sliding and basal slip

220 which characterize the flow of ice. All three creep regimes are implemented to calculate a range
221 in T_b. Only the grain boundary sliding (GBS) regime is dependent on grain size, in which a range
222 from 1mm to 10cm (appropriate for a convecting ice mantle in which grain size has reached
223 equilibrium) was used (Barr and McKinnon 2007).
224 T_b also depends on the strain rate $\dot{\varepsilon}$, the gas constant R, grain size d, and the shear
225 modulus μ, which is calculated from v and E used in equation (1). A value of 0.01 for the
226 Deborah number, De, has been shown by Mancktelow (1999) to be the transitional value
227 between elastic and viscous behavior. Table 1 summarizes of all the values used for our
228 calculation.
229 To estimate the strain rate we need to know the horizontal extension. To achieve this we
230 measured the throw of the fault from the topographic profiles. Normal faults typically dip at
231 60° (Turcotte and Schubert 2002) so by dividing twice the throw by the tangent of the dip angle
232 the local horizontal extension can be inferred. The strain can then be estimated by dividing the
233 fault extension by the distance to the next adjacent graben, as the strain is maximum above a
234 fault and gradually decreases perpendicular to the strike. Taking a representative value of 3 km
235 for the throw and 150 km for the distance between graben, we obtain a strain value of **0.024** at
236 the time of formation. The faster a terrain forms, the higher the required heat flux, thus we chose
237 upper and lower bounds of 3Gyr and **1Myr** for our timescale, producing corresponding upper
238 and lower bound strain rates of 10^{-19}s^{-1} and $\mathbf{10^{-15}\,s^{-1}}$, respectively.
239 Employing all three different creep mechanisms with these assumed strain rates, the
240 temperature found at the base of the elastic layer, T_b using Equation 3, ranges from 99 to 146 K.
241 The thermal gradient of Ariel's ice is then related to the heat flux, F, by the thermal conductivity,
242 k, as stated by Fourier's law.

243 $$F = k\frac{(T_b - T_s)}{t_e} \qquad (4)$$

244 The thermal conductivity depends on the composition and temperature of the material.
245 The thermal conductivity of ice varies as $567/T$ (Klinger 1980), so for the cold near-surface
246 conditions appropriate to Ariel, we take k=5 Wm^{-1}K^{-1}. We take a surface temperature, T_s of 75
247 K, so that for t_e=3.8-4.4 km we obtain heat fluxes between 28-92 mW/m^2 at the time of
248 formation.
249

5. Discussion

The source of energy needed to produce our inferred heat fluxes is not well-understood. The amount of internal energy generated by radioactive decay, assuming a chondritic composition for the silicate core and a silicate mass fraction of 0.56, is only 5-8 mW/m^2 shortly after formation, and today only produces 0.6-1 mW/m^2 (Hussmann et al., 2010). Combined with accretionary energy, it is possible that this could account for some resurfacing. Even so, Umbriel shares a similar size and density but appears to be geologically undisturbed. As such, it seems more likely that the source of endogenic heat is due to an episode of tidal heating at some point in Ariel's orbital history.

In the case of a synchronously rotating satellite, stress from the planet's gravitational field distorts the satellite into an ellipsoidal shape and the eccentricity of the orbit causes oscillations of this deformation, which can result in dissipation of tidal energy (Peale, 1999). The rate of dissipation, and corresponding heat flux, depends on k_2/Q. The satellite's second-degree Love number, k_2 describes the rigidity and the response of the body to tidal forces. Ariel is most likely differentiated and k_2 could be calculated numerically for a multilayered body (e.g. Roberts and Nimmo 2008). However, for small satellites, the predicted k_2 value for a homogeneous body can be used as an adequate approximation (Peale, 1999).

$$k_2 = \frac{3/2}{1 + \frac{19\mu}{2\bar{\rho} g r_s}} \quad (5)$$

$\bar{\rho}$ is the bulk density, g is the gravitational acceleration, r_s is the satellite radius and μ is the rigidity. **Q is the tidal dissipation factor; we used a broad range of 10 – 1000 given that the internal structure of Ariel is poorly understood. The Q values are based on Goldreich and Soter (1966). When using 3GPa for the rigidity of ice, the predicted k_2/Q values range between of 1.4×10^{-3} –1.4×10^{-5}.** The tidal dissipation for a synchronous satellite in an eccentric orbit is given by (Peale 1999):

$$E_t = -\frac{21}{2}\frac{k_2}{Q}\frac{(\omega r_s)^5}{G}e^2 \quad (6)$$

In Equation 6, G is the gravitational constant, ω the orbital frequency (mean motion) and e the current orbital eccentricity. We can use the inferred heat fluxes to solve for k_2/Q given the

eccentricity (Ariel's current eccentricity is 0.0034). At the present eccentricity, the k_2/Q needed to produce our observed heat fluxes of 28-92 mW/m^2 corresponds to k_2/Q in the range of 0.05-0.17. This is a factor of over 10 to 100 more than the predicted value for a homogenous Ariel, indicating that present-day tidal heating is unlikely to be responsible for the inferred heat fluxes. Ariel could potentially possess a convecting ice mantle or a subsurface ocean; these could lower the effective rigidity and allow for a higher tidal deformation, which increases k_2/Q (Zhang and Nimmo 2009). But k_2/Q would still need to increase by 1-2 orders of magnitude higher than predicted, implying that the observed heat flux is more likely a remnant of an earlier eccentricity.

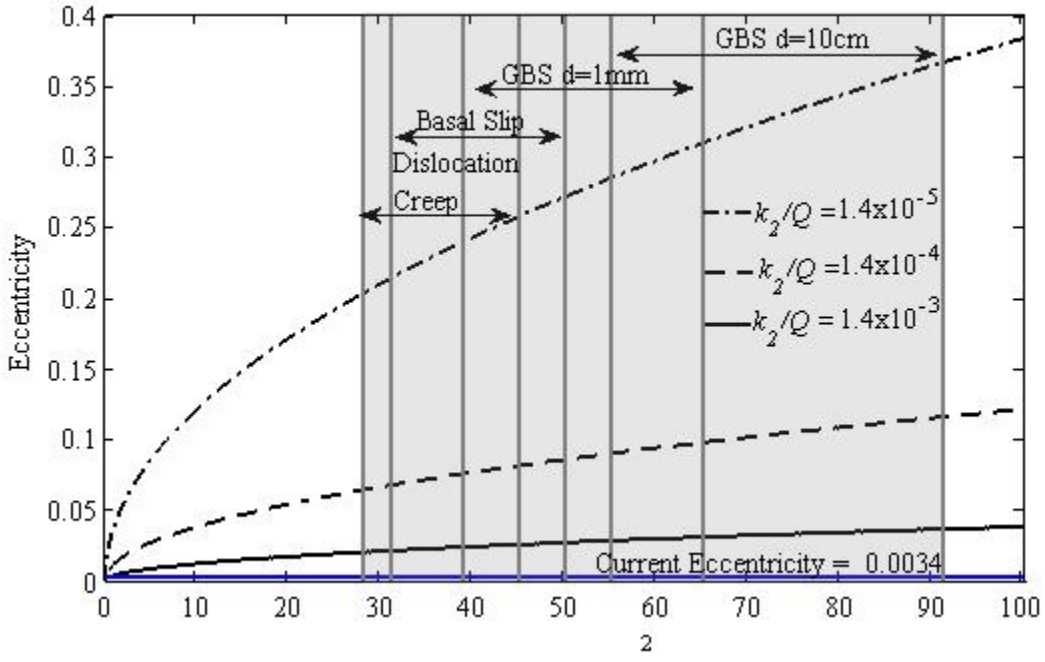

Figure 3. The eccentricity required to produce a given heat flux from tidal heating, based on equation 6 and using a Q range of 10-1000. Our inferred heat fluxes fall between 28-92 mW/m^2 and are represented by the grey shaded region, which is further subdivided in sections based on the ice rheology. The blue line shows how much tidal heat is produced at Ariel's current eccentricity for a range of different k_2/Q values.

The required eccentricity for a given heat flux, ice rheology and predicted k_2/Q are shown in Figure 3. Our inferred heat flux values are in the range of 28-92mW/m^2, which results in required eccentricities between 0.02 and 0.37. The above results imply that a high, ancient eccentricity could have generated the inferred heat fluxes. However, the problem is sustaining these high required eccentricities for long enough to cause global deformation; when tidal

297 dissipation is high, energy is removed from the system and the orbit will begin to circularize
298 (Dermott et al., 1988). In the absence of a resonance, the time for Ariel's orbit to circularize is
299 given by

300
$$t = -\frac{2}{21}\frac{m_a}{m_U}\left(\frac{a_a}{r_s}\right)^5\left(\frac{1}{\omega}\right)\left(\frac{Q}{k_2}\right) \quad (7)$$

301 The subscripts correspond to either Ariel's or Uranus' dynamical properties with *m* being the
302 mass, ω the mean motion and *a,* the semi-major axis. Using Ariel's current semi-major axis and
303 k_2/Q of 1.4×10^{-4} results in a timescale of 1.7 Myr for the orbit to damp **in the absence of**
304 **excitation mechanisms. A high primordial eccentricity would thus damp rapidly. This**
305 **outcome is inconsistent with the observation that the graben post-date the cratered terrain,**
306 **unless the cratered terrain formed extremely rapidly (<1 Myr) - which seems unlikely – or**
307 **the eccentricity was excited at a later date.**

308 Consequently, forced eccentricities from ancient mean motion resonant configurations
309 have been suggested as a possible heating source for Ariel. Tittemore and Wisdom (1989)
310 predicted a number of mean motion resonances between the Uranian satellites as their orbits
311 evolved outwards from tidal dissipation in Uranus. A 5:3 mean motion resonance between Ariel
312 and Miranda is possible if the *Q* of Uranus is ≤ 12,000. Passage through this resonance leads to
313 large variations in both Miranda and Ariel's orbits. For Miranda, the eccentricity suddenly
314 jumps to 0.02 but then gradually decreases until it escapes the resonance. However, the effect on
315 Ariel is much less significant, since its mass is larger than Miranda, with its highest eccentricity
316 reaching only 0.007 at a corresponding semi-axis of 1.71×10^5 km.

317 The most probable resonance is an Ariel and Umbriel 2:1 mean motion commensurability
318 that would have been encountered at 4.26 Ga if *Q* of Uranus is ≤ 11,000 and pre-resonant
319 eccentricities were comparable to their current values (Tittemore &Wisdom, 1989). When
320 captured into this resonance, the eccentricity of Ariel will have grown until reaching a stable
321 configuration, with an equilibrium eccentricity of 0.02. Furthermore, Tittemore (1990) found that
322 capture into 4:1 Ariel and Titania resonance at 3.8 Ga would have increased the orbital
323 eccentricity of Ariel considerably, reaching eccentricities up to 0.03-0.04 at time of escape,
324 which could possibly lead to important tidal heating. The *Q* for Uranus would have to have been
325 in the range 11,000-13,000 and Ariel's pre-capture eccentricity would have to have been smaller

than it currently is. A secondary resonance would have forced the satellites into a chaotic zone, ultimately leading to its disruption.

The equilibrium power that is dissipated through a two-body resonance is given by:

$$H = \omega T \left[1 - \frac{\left(1+\frac{m_2 a_1}{m_1 a_2}\right)}{\left(1+\frac{m_2}{m_1}\sqrt{\frac{a_2}{a_1}}\right)}\right] \quad (8)$$

where m_1 and m_2 are the mass of the inner and outer satellites respectively and a_1 and a_2 are the corresponding semi-major axes at time of resonance (Lissauer et al. 1984). The tidal torque, T, on Ariel, is found by (Peale, 1999)

$$T = \frac{3}{2}\frac{k_{2U} G m_a^2 r_U^5}{a_a^6 Q_U} \quad (9)$$

Here Q_U, k_{2U} and r_U correspond to the dynamical properties of Uranus; thus our **uncertainty in** the mechanical properties and structure of Ariel does not cause any uncertainty in the rate of tidal heating as long as the eccentricity is in equilibrium **(Meyer and Wisdom 2007). Note, however, that a *Q* for Uranus <11,000 would result in higher equilibrium heating rates, although *Q* is unlikely to be less than 9000 by analogy to Neptune (Zhang and Hamilton 2008). Whether equilibrium eccentricity is attained depends on the competing timescales of eccentricity damping and thermal adjustment (Ojakangas and Stevenson 1986). Given the short eccentricity-damping timescales derived above (eq. 7), equilibrium eccentricity appears to be a reasonable assumption.**

As summarized in Table 2, the results show that all the potential resonances are incapable of producing sufficient tidal dissipation to be responsible for Ariel's resurfacing. The highest heat flux is produced from 4:1 resonance, and this, even with the addition of radioactive decay, only yields a total heat flux of 12mW/m^2. This is less than half of the minimum required power inferred from the flexural profiles. Thus, we conclude that passage through any of these resonances is unlikely to have been responsible for the inferred heat fluxes.

Ariel's evolution may have shared something in common with that of the Saturnian satellite Dione; both share similar size, density, surface temperatures and compositions. Dione has a radius of 560km and density of 1480 kg/m^3, and is composed of mainly water ice (Ariel's radius is 580km and has a density of 1660 kg/m^3). Dione shows evidence of geological activity

with numerous extensional faults and possible cryovolcanic deposits, similar to those on Ariel, and thus can be a useful comparison for evaluating our results (Wagner et al., 2009). In Hammond et al. (2013), apparent flexural features on Dione were used to estimate local elastic thickness, which resulted in values of 3.5 ± 1 km with corresponding heat fluxes between 25-60mW/m^2. The broad similarity between these two bodies helps to strengthen our confidence in our inferred values. Similarly, rift flank uplift at Miranda, another deformed Uranian satellite, resulted in elastic thickness estimates of about 2km (Pappalardo et al. 1997), which is within a factor of 2 of our result and also suggests an episode of elevated heat flux.

Since the terrain on Ariel does not show large variations in crater density, and deformation of the crust is observed globally, it seems likely that our t_e and heat flux values are representative of Ariel's past global value, rather than simply a local, enhanced heat flux. Furthermore, the small strains inferred (~1%) and large area subjected to extension suggest that the local heat fluxes inferred are representative of the average thermal state of the shell at the time of deformation. On the other hand, we assumed a perfectly elastic lithosphere, which is an oversimplification as there might be **either** long-term relaxation (Damptz and Dombard 2011) **or yielding and/or fracturing in the near-surface. Both effects would cause our heat flux estimates to be too high; quantification of these effects is not straightforward but should be a priority for follow-on work.**

It may be important to consider the role of impurities and their effect on the thermal behavior of ice. Grundy et al. (2006) spectrally observed the presence of CO_2 ice on the trailing hemisphere of Ariel. The inclusion of other volatiles on Ariel will weaken the ice, resulting in lower viscosities than pure ice at the same temperature. This allows for easier mobilization and enables milder tidal heating episodes to cause the same surface **deformation (cf. Passey 1983). Thus, if Ariel's ice shell contains a significant fraction of volatiles and *Q* of Uranus is near the lower bound, the hypothesized resonances could potentially have been enough to cause the tectonic deformation.** Alternatively, the near-surface ice could be porous and thus of lower thermal conductivity. **On Ariel, the depth of the low thermal conduction layer will be larger compared to icy satellites like Europa or Ganymede due to its lower gravity.** Such an insulating layer would permit lower heat fluxes for the same elastic thickness (equation 4; see also Bland et al. 2012). On the other hand, the thickness of a porous layer is self-limiting,

because such pores will tend to compact under overburden pressure if they become too warm (Besserer et al. 2013).

6. Conclusion

The surface geology on Ariel suggests an episode of relatively high heat fluxes causing the observed resurfacing, crater relaxation and perhaps extrusion of material. Our flexural profiles (Figure 2) indicate that the elastic thickness was between 3.8 - 4.4 km at the time of formation, constraining the heat flux to be in the range 28-92 mW/m^2. The required eccentricities to generate this heat flux fall between 0.02-0.37, much higher than the current value. Possible mean motion resonances between Umbriel, Titania and Miranda would have increased Ariel's eccentricity in the past; however, we found that the resulting equilibrium heat fluxes produced were not enough to account for the inferred heat fluxes. The 4:1 Ariel-Titania resonance produced the highest values of 4.3 mW/m^2 but even with radioactive decay it produces less than half of the minimum inferred heat flux. Thus, the origin of Ariel's resurfacing remains unexplained.

Parameter	Value	Equation	Reference
g	0.27 m/s^2	2,5.	(Peale,1999)
E_{ice}	9 GPa	2.	(Gammon, 1983)
ν_{ice}	0.33	2.	(Gammon, 1983)
$\Delta\rho$	1000 kg/m^3	2.	(Gammon, 1983)
Q_a	49 kJ/mol	3.	(Goldsby & Kohlstedt, 2001)
A	3.9 x $10^{-3} MPa^{-1.8} m^{1.4} s^{-1}$	3.	(Goldsby & Kohlstedt, 2001)
n	1.8	3.	(Goldsby & Kohlstedt, 2001)
d	1mm	3.	(Goldsby & Kohlstedt, 2001)
p	1.4	3.	(Goldsby & Kohlstedt, 2001)
De	0.01	3.	(Mancktelow, 1999)
μ	3 GPa	3,5.	(Goldsby & Kohlstedt, 2001)
R	8.3145 J $k^{-1}mol^{-1}$	3.	(Goldsby & Kohlstedt, 2001)
k	5 $Wm^{-1}K^{-1}$	4.	(Klinger 1980)
$\bar{\rho}$ $\overline{\rho}$	1660 kg/m^3	5.	(Peale 1999)
r_s	580km	5,6,7.	(Peale 1999)
Q	10-1000	6,7.	(Goldreich &Soter,1966)
e	0.0034	6.	(Peale 1999)
ω	$2.9x10^{-5} sec^{-1}$	6,7	(Peale 1999)
a_a	$1.91x10^8$ m	7,8,9	(Peale 1999)
m_a	$1.353x10^{21}$kg	7,8,9	(Peale 1999)
m_U	$8.663x10^{25}$kg	7,9	(Peale 1999)

m_m	0.66×10^{20}kg	8.	(Tittemore, 1990)
m_u	1.17×10^{21} kg	8.	(Tittemore & Wisdom, 1989)
m_t	3.52×10^{21}kg	8.	(Tittemore, 1990)
r_U	2.53×10^{7} m	9.	(Peale 1999)
k_{2U}	0.103	9.	(Tittemore, 1990)

Table 1. List of parameters used for Equations 1-9. Subscripts *a, u, m, t*and *U* refer to Ariel, Umbriel, Miranda and Uranus respectively.

Resonance	Heat Flux (mW/m^2)
5:3[a] Miranda-Ariel	2.7
2:1[b] Ariel-Umbriel	0.6
4:1[c] Ariel-Titania	4.3

[a] $a_a = 1.65 \times 10^5$km, $a_m = 1.73 \times 10^5$km, Q_U=12,000

[b] $a_a = 1.60 \times 10^5$km, $a_u = 1.72 \times 10^5$km, Q_U=11,000

[c] $a_a = 1.67 \times 10^5$km, $a_t = 4.21 \times 10^5$km, Q_U=11,000

Table 2. A summary of the tidal heat fluxes produced for each resonance. The heating rate was calculated by using Equations 8 and 9. The rest of the dynamical properties are listed in Table 1.

References

Barr, A.C., McKinnon, W.B., 2007. Convection in ice I shells and mantles with self-consistentgrain size. *J. Geophys. Res.,* 112, E02012.

Besserer J., Nimmo F., Roberts J.H., Pappalardo R.T., 2013. Convection-driven compaction as a possible origin of Enceladus's long wavelength topography. *Journal of Geophysical Research* 118, Issue 5, pages 908–915.

Billings, S.E., Kattenhorn, S.A., 2005. The great thickness debate: Ice shell thickness models for Europa and comparisons with estimates based on flexure at ridges. *Icarus* 177, 397–412.

Bland M.T., Singer K.N., McKinnon W.B., Schenk P.M. 2012. Enceladus' extreme heat flux as revealed by its relaxed craters. *Geophys. Res. Lett.* 39, L17204.

Damptz, A.L., Dombard, A.J., 2011. Time-dependent flexure of the lithospheres on the icy satellites of Jupiter and Saturn. *Icarus* 216, 86–88.

Dermott, S.F., Malhotra, R. and Murray, C.D., 1988. Dynamics of the Uranian and Saturnian satellite systems: a chaotic route to melting Miranda? *Icarus* 76, 295–334.

Dombard, A.J., McKinnon, W.B., 2006. Elastoviscoplastic relaxation of impact crater topography with application to Ganymede and Callisto. *J. Geophys. Res.* 111, E01001.

Gammon, P.H.,H. Kiefte, and M.J. Clouter, 1983. Elastic constants of artificial and natural ice samples from brillouin spectroscopy. *Journal of Physical Chemistry*, 87, 4025-9.

Giese, B., Wagner, R., Hussmann, H., Neukeum, G., Perry, J., Helfenstien, P., Thomas, P.C., 2008. Enceladus: An estimate of heat flux and lithospheric thickness from flexurally supported topography. *Geophys. Res. Lett.* 35, L24204

Giese, B., Wagner, R., Neukum, G., Helfenstein, P., Thomas, P.C., 2007. Tethys: Lithospheric thickness and heat flux from flexurally supported topography at Ithaca Chasma. *Geophys. Res. Lett*. 34, L21203.

Goldreich and Soter,1966. Q in the Solar System, *Icarus* 5: 375-389

Goldsby, D.L., Kohlstedt , D.L., 2001. Superplastic deformation of ice: Experimental observations. *J. Geophys. Res.* 106, 11017-11030

Grundy W.M, Young L.A, Spencer J.R, Jofhnson R.E, Young E.F, Buie M.W,. 2006. Distributions of H_2O and CO_2 ices on Ariel, Umbriel, Titania and Oberon from IRTF/SpeX observations, *Icarus* 184, 543-555.

Hammond, N.P, Phillips C., Nimmo F, and Kattenhorn S., 2013. Flexure on Dione: Investigating subsurface structure and thermal history, *Icarus* 223 418-422,

Hussmann, H., F. Sohl, and T. Spohn (2006), Subsurface oceans and deep interiors of medium-sizedouter planet satellites and large trans-neptunian objects, *Icarus*, 185, 258–273

Hussmann, H , Choblet, G., Lainey, V., Matson, D. L., Sotin, C., Tobie, g., Van Hoolst, T (2010)/ Implications of rotation, orbital states, energy sources, and heat transfer for internal processes in icy satellites. *Space Sci. Rev.*153, 317-348.

Hurford, T.A., Beyer, R.A., Schmidt, B., Preblich, B., Sarid, A.R., Greenberg, R., 2005. Flexure of Europa's lithosphere due to ridge-loading. *Icarus* 177, 380–396.

513 Jankowski D.G and Squyres S.W., (1991) Sources of error in planetary photoclinometry, *J.*
514 *Geophys. Research*, 96, Issue E4, pages 20907–20922
515
516 Johnson T.V., 2005. Geology of Icy Satellites. *Space Science Reviews,* 116 Issue 1-2 pp. 401-
517 420
518
519 Klinger, J., 1980. Influence of a phase transition of ice on the heat and mass balance of comets.
520 *Science* 209, 271–272.
521
522 Lissauer J.J, Peale S.J and Cuzzi J.N, 1984. Ring torque on Janus and the melting of Enceladus,
523 *Icarus* 58: 159-168.
524
525 Mancktelow, N.S., 1999. Finite-element modelling of single-layer folding in elasto- viscous
526 materials: The effect of initial perturbation geometry. *J. Struct. Geol.* 21,
527 161–177.
528
529 Meyer J, Wisdom J., 2007 Tidal heating in Enceladus, *Icarus* 188 535 -539
530
531 Miller E. *Uranus: the planet, rings and satellites.* John Wiley, New York, 1998
532
533 Nimmo F. and Pappalardo R.T., 2004. Furrow flexure and ancient heat flux on Ganymede
534 *Geophys. Res. Lett.* , 31, L19701 doi:10.1029/2004GL020763
535
536 Nimmo F., Pappalardo R.T, Geise B. 2002. Elastic thickness and heat flux estimates on
537 Ganymede, *Geophys. Res. Lett.,* 29(7), 1158, 10.1029/2001GL013976
538
539 Nyffenegger P., Davis D.M, and Consolomagno G.J, 1997. Tectonic lineations and frictional
540 faulting on a relatively simple body (Ariel). *Icarus* 45, Issue 9, pages 1069-1080
541
542 Ojakangas G.W., Stevenson D.J., 1986. Episodic Volcanism of Tidally Heated Satellites with
543 Applications to Io. *Icarus* 66 341-358
544
545 Pappalardo, R.T., Reynolds S.J., and Greeley, R., 1997. Extensional tilt blocks on Miranda:
546 Evidence for an upwelling origin of Arden Corona. *J. Geophys. Res*. 102, 13369-13379.
547
548 Pappalardo R.T. and 15 co-authors, 1998, Grooved terrain on Ganymede: First results from
549 Galileo high-resolution imaging, *Icarus* 135, 276-302.
550
551 Passey Q.R., 1983. Viscosity of the Lithosphere of Enceladus., *Icarus* 53, 105 -120
552
553 Peale, S.J. 1999.Origin and evolution of the natural satellites, *Annual Review of Astronomy and*
554 *Astrophysics,* 37, 533-588
555
556 Plescia, J.B., Boyce, J.M., 1987. Geology and cratering history of Ariel, *In its Reports of*
557 *Planetary Geology and Geophysics Program , 1986 p 19-21*
558

559 Roberts J.H, Nimmo F., 2008. Tidal heating and the long-term stability of a subsurface ocean on
560 Enceladus, *Icarus* 194 675-689
561
562 Schenk, P. M., 1989.Crater formation and modification on the icy satellites of Uranus and
563 Saturn: Depth/diameter and central peak occurrence. *Journal of Geophysical Research*Volume
564 94, Issue B4, pages 3813–3832,
565
566 Schenk P.M, 1991. Fluid volcanism on Miranda and Ariel. *Journal of Geophysical Research,*
567 *96,* 1887-1906
568
569 Schenk, P.M., 2009. Slope characteristics of Europa: Constraints for landers and radar sounding.
570 *Geophys. Res*. Lett., 36, doi:10.1029/2009GL039062.
571
572 Schenk, P.M., and W.B. McKinnon, 1988. Viscous relaxation of craters on Ariel: Implications
573 for crustal composition, *Bull. Am. Astron. Soc.,* 20, 881.
574
575 Schenk, P.M., Pappalardo, R.T., 2004. Topographic variations in chaos on Europa:
576 implications for diapiric formation. *Geophysical Research Letters* 31,
577 L16703.
578
579 Turcotte. D.L., and G. Schubert, *Geodynamics*, 450 pp., John Wiley, New York, 2002
580
581 Tittemore,W.C,. 1990. Tidal heating of Ariel *Icarus*, 87, 110–139
582
583 Tittemore W.C. and Wisdom J., 1989. Tidal evolution of the Uranian satellites I. Passage of
584 Ariel and Umbriel through the 5:3 mean-motion commensurability *Icarus*, 74, 172–230
585
586 Wagner, R.J., Neukum, G., Stephan, K., Roatsch, T., Wolf, U., Porco, C.C., 2009. Tectonic
587 features on Saturn's satellites Dione and Rhea: Morphology and stratigraphy derived from
588 Cassini ISS images. *Lunar Planet. Sci.* XL. Abstract 2142.
589
590 Weissel, Jeffrey K, Karner, Garry D. 1989. Flexural uplift of rift flanks due to mechanical
591 unloading of the lithosphere during extension, *Journal of Geophysical Research*, Vol. 94, No.
592 B10. pp. 13919-13950
593
594 Zhang, K., Hamilton D.P. 2008. Orbital resonances in the inner Neptunian system II. Resonant
595 history of Proteus, Larissa, Galatea and Despina. *Icarus* 193, 267-282.
596
597 Zhang K., Nimmo F., 2009. Recent orbital evolution and the internal structures of Enceladus and
598 Dione, *Icarus* 204 597-609
599
600
601
602
603
604

605
606
607
608
609
610
611